



POLITECNICO
MILANO 1863

DIPARTIMENTO DI MECCANICA



Role of elongational viscosity of feedstock in extrusion-based additive manufacturing of powder-binder mixtures

Kedarnath Rane, Thierry Barriere & Matteo Strano

This is a post-peer-review, pre-copyedit version of an article published in The International Journal of Advanced Manufacturing Technology. The final authenticated version is available online at: <http://dx.doi.org/10.1007/s00170-020-05323-9>

This content is provided under [CC BY-NC-ND 4.0](https://creativecommons.org/licenses/by-nc-nd/4.0/) license



Role of elongational viscosity of feedstock in extrusion-based additive manufacturing of powder–binder mixtures

Kedarnath Rane^a, Thierry Barriere^b, Matteo Strano^{a*}

^a Dipartimento di Meccanica, Politecnico di Milano, Via La Masa 1, 20159 Milan, Italy

^b Univ. Bourgogne Franche-Comté, FEMTO-ST Institute, CNRS/UFC/ENSMM/UTBM, Department of Applied Mechanics, 25000 Besançon, France

* Corresponding author. tel: +39-0223998534, e-mail: matteo.strano@polimi.it,

ORCID: 0000-0003-3652-9320

Abstract

The 3D printing of metals and ceramics by the extrusion of a powder/thermoplastic binder feedstock is an extrusion-based additive manufacturing (EAM) technique, and has received significant interest. EAM feedstocks are generally characterised by their shear viscosity. A quantitative comparison with the shear flow data, through an estimation of the Trouton ratio, indicates that the extensional viscosities are three orders of magnitude greater than their shear flow viscosity at a comparable shear rate obtained in three different high-loaded polymers retained for this study. This experimental study addresses the unsolved issue of the role of elongational viscosity in the modelling of EAM of highly viscous melts. The study was conducted using three feedstocks with a water-soluble binder and high powder loading. The different powder materials used for this study are stainless steel, alumina, and zirconia. Initially, the rheological properties of the feedstocks were assessed using capillary rheometers. A pressure drop model based on the shear and elongational components of the viscosity was proposed to predict the extrusion pressure during capillary tests. The model was adapted to develop a specific EAM machine, namely an EFeSTO, equipped with a pellet extrusion unit. Experimental EAM tests were conducted, and the pressure drops were analytically predicted and experimentally measured. A total of 31 different combinations of extrusion velocities, nozzle diameters, 3D printed shapes, and materials were tested through a total 184 experimental runs. The model predicts well the experimental pressures for the steel feedstock, whereas it underestimates the pressure for the two ceramic feedstocks owing to their different thermal properties. The results of this study clearly demonstrate that the pressure, and therefore the material flow during the EAM processes of viscous materials, cannot be modelled well without considering the elongational viscosity.

Keywords: 3D printing; highly viscous melt; extrusion pressure; elongational viscosity

1 Introduction

Powder injection moulding (PIM) is a convenient widespread manufacturing process for producing complex components in large batches [1]. It employs a feedstock usually composed of a thermoplastic polymeric binder, filled with metals or a ceramic powder. This type of feedstock can also be used for extrusion-based additive manufacturing (EAM) technologies for metallic and ceramic components [2]. There are two types of EAM technologies. One is called direct ink writing (DIW), which has also been called robocasting, based on the direct use of a powder-binder/matrix slurry feedstock (without increasing the temperature for melting) [3]. The other is called fused filament deposition (FFD). It is a 3D printing process or additive manufacturing technique that applies a continuous filament. A filament-type thermoplastic polymer is melted before it extrudes from the nozzle and is deposited on the growing specimen. The headed printer extruder heat usually moves in two dimensions to deposit one horizontal layer at a time. The specimen or printer extruder head is then moved vertically by a small amount to begin a new layer. To realise a 3D component with a functional material, Nadernezhad et al. [4] investigated the extrusion of PLA/CNT nano-composites dedicated to additive manufacturing using this FFD process. In our case, the FFD process has been modified for application with pellets instead of a filament using the EAM of powder-binder mixtures.

Some EAM machines for the processing of such feedstocks are commercially available (including Markforged Metal X and Desktop Metal Studio); however, no commercial machines are yet available for extrusion starting from the pellets of feedstock, instead of filaments or rods. EAM machines based on the extrusion of pellets allow for material diversity and are cost effective.

The EFeSTO machine has been previously developed and was employed in this study. It combines a servo-controlled small pellet extruder unit with a robotic deposition table based on parallel kinematics [5]. One advantage of EFeSTO for the present study is that the torque (and therefore the pressure) applied by the pellet extrusion unit can be monitored during the processing.

Melt viscosity [6] is one of the important characteristics of a feedstock and is used to predict the rheological behaviour during highly viscous melt extrusion and in the correct design of a 3D printing process through the selection of appropriate extrusion parameters.

In previous studies associated with powder injection moulding, the rheology of highly loaded feedstocks has generally been assessed through a capillary rheometer, used to characterise the shear viscosity behaviour [7]. A literature review dedicated to the laws of highly concentrated feedstock alloys is available in [8], where a shear viscosity model was proposed for superalloy powders. A capillary rheometer is generally preferred over other rheometers to reduce the estimation errors from a wall slip [9]. The shear

viscosity is universally and correctly considered the most important parameter for highly viscous PIM feedstocks. However, during the EAM processes, the shear rates are comparably smaller and the extrusion nozzles are shorter; therefore, compared to PIM, EAM processes induce a comparably lower amount of shear deformation, whereas the extruded filaments inevitably elongate. In a review on the EAM processes [10], the extensional viscosity was not mentioned. In a more recent review [11], the author recognised that elongational viscosity is generally accepted as an important parameter for determining the pressure drops in additive manufacturing through a material extrusion. However, despite this common belief, the characterisation of the elongational viscosity in scientific papers dealing with the EAM processes has generally been neglected. In [12], the authors list all of the relevant feedstock properties for the EAM of metals, and place a large emphasis on the shear viscosity, while neglecting to mention the elongational component. The shear viscosity is still frequently considered a unique or important property of highly viscous EAM feedstocks, such as in [13], where the authors studied the EAM of zirconia, or in [14], where the authors studied the effects of the powder size on the properties of highly filled polymers for fused filament deposition (FFD). In [15], the authors characterised the viscosity of highly viscous polymers for FFD and recognised the importance of the material at extremely small or “zero” shear rates; nevertheless, they modelled and represented the shear viscosity only, and not the elongational viscosity.

One of the reasons why the elongational or entrance viscosity of viscous non-Newtonian fluids during the EAM processes has been neglected by the scientific literature is the inherent difficulty of knowing the instantaneous extrusion pressure during such processes, or even worse, the instantaneous shear stress. In typical FFD machines, the instantaneous extrusion pressure is unknown. As an exception, in [16] the authors conducted a very interesting study using in-line rheological pressure measurements in FFD. However, they did not characterise or isolate the extensional viscosity.

The purpose of the present study is to demonstrate that, for EAM with specific viscous melts, which take place at a low shear rate and within relatively short extrusion nozzles, the characterisation of the feedstock based on the elongational viscosity is more important than the shear viscosity when predicting the flow.

The remainder of this paper is organised as follows: In the next section, the relevant rheological models are presented, highlighting the differences between the shear and elongational viscosity. The experimental materials, methods, and equipment are then described. In the third section, the rheological model is validated based on capillary rheometer data. Finally, the results of extrusion and 3D printing tests using EFeSTO equipment are presented and discussed.

2 Rheological models

The rheology of powder-binder feedstocks has been extensively studied and many models have been proposed to describe the melt viscosity during the extrusion and injection moulding processes. The well-known constitutive equation for the shear viscosity of Newtonian fluids is as follows:

$$\eta_s = \frac{\tau}{\dot{\gamma}} \quad (1)$$

where τ is the shear stress and $\dot{\gamma}$ is the applied shear rate. In addition, η_s is the shear viscosity or the resistance of the fluid to shearing. The shear viscosity is a constant for Newtonian fluids, whereas the powder-binder feedstocks usually show a non-Newtonian characteristic [17]. In PIM applications, a shear-thinning (or pseudoplastic) effect is observed, where the shear viscosity decreases upon an increase in the shear rate [18]. The simplest way to describe a pseudoplastic effect is the power-law model, which demonstrates a non-linear relation between the shear stress and shear rate as follows:

$$\tau = K\dot{\gamma}^n \quad (2)$$

where K and n are material-specific parameters, namely, the consistency and shear rate sensitivity, respectively. The shear rate sensitivity n is the power-law index, which is $n < 1$ for pseudoplastic fluids; shear-thinning then becomes more evident with a decrease in n . In a previous study [6], it was demonstrated that larger K -values favour a better stability of the extrusion of the metal-binder feedstocks, in terms of both the pressure signal and filament quality.

Experimental measurements of the shear viscosity can be conducted using a variety of instruments, given the wide range of viscosities that feedstock materials can present [19]. The most common are capillary rheometers, which can be used from 2 to 3,000 s⁻¹ [20]. For a capillary rheometer, pressure is applied using a piston, and the apparent shear rate ($\dot{\gamma}_a$) and shear stress at the wall (τ_w) are determined from the extruded flow rate for non-Newtonian fluids:

$$\tau_w = \frac{\Delta P_{cap}}{L/2R}, \quad (3)$$

$$\dot{\gamma}_a = \frac{4Q}{\pi R^3}, \quad (4)$$

where ΔP_{cap} is the pressure drop at the capillary, L is the capillary length, R is the radius, Q is the volumetric flow rate, and $\dot{\gamma}_a$ is the apparent shear rate, i.e. the true shear rate of a Newtonian fluid. For shear-thinning fluids, Rabinowitsch's correction for determining a more realistic value of the true shear rate $\dot{\gamma}_w$ must be employed [21]:

$$\dot{\gamma}_w = \frac{(3n+1)4Q}{4n\pi R^3}. \quad (5)$$

Nozzles used in EAM machines for highly viscous polymers [2] are generally extremely short, with length over diameter (L/D) ratios of well below 10. For short capillaries ($L/D < 25$), an additional pressure drop ΔP_e at the entrance must be accounted for owing to the sharp decrease in diameter from the barrel where the material is compressed before entering the capillary. Bagley's correction is often used for this purpose [17]:

$$n_B = \frac{\Delta P_e}{2\tau_w} \quad (6)$$

Bagley's corrected shear stress at the wall can be calculated as follows:

$$\tau_w = \frac{(\Delta P_{cap} + \Delta P_e)}{2(L/R + n_B)} \quad (7)$$

Bagley's correction depends on both the geometry of the capillary and the material characteristics. The role of the entrance pressure drop in the short capillaries has been considered by many authors to be related to the so-called elongational or extensional viscosity [22]. Indeed, for a deeper understanding of the rheological of the feedstock during the extrusion process of EAM, the contributions of the shear viscosity and the elongational viscosity need to be explicitly quantified. Numerous models have been proposed to describe the elongational viscosity of polymer melts, e.g., using a flow through a tube with an abrupt contraction as a measure [23]. For elongational rheometry experiments of non-Newtonian fluids, the elastic and viscous contributions can be separated [24]. When characterising highly viscous materials, the roles of the capillarity and gravity are generally neglected.

One of the most accredited models for estimating the entrance pressure drop (ΔP_e) was developed by Cogswell [25], who assumed that the pressure drop can be modelled by defining the shear viscosity (η_s) and elongational viscosity (η_E) dependent terms [26]. This model is only accurate at low deformation rates (as in EAM applications). As an alternative to Cogswell's model, Binding and Gibson's model [27] can also be used to accurately describe the pseudoplastic effect of PIM feedstock over a wide range of shear rates when considering the contributions of the shear and elongational viscosity. A simple rheological model, comparable to Binding and Gibson's model, is proposed herein to analyse the results of twin bore capillary rheometers.

2.1 Rheology of feedstock: Shear and elongational viscosities

Polymer processing through the mixing and printing of a high loaded polymer usually involve medium and large strain rates in shear and extensional flows, and the viscosity of the feedstock depends on the binder composition and properties of the powders, mixing parameters, and conditions. In the case of a high loaded

polymer, Arabo [28] concluded that an extensional (or elongational) flow is important and has therefore attracted significant interest in the powder forming processes.

In a twin bore rheometer, there are two nozzles: The nozzle on the left is a long capillary ($L/D \gg 10$), and the nozzle on the right has a negligible length, i.e., virtually a “zero shear” deformation. A simple model has been developed based on the data obtained from a twin-bore capillary rheometer. This model was then validated, as shown later in this paper, on a different twin-bore rheometer with a different L/D ratio. The model assumes that the total pressure at a long (left) capillary is considered as the sum of two components as follows:

$$P_{tot} = \Delta P_{left} = \Delta P_{ent} + \Delta P_{cap}, \quad (8)$$

where ΔP_{ent} is the entrance pressure variation owing to the abrupt change in section between the barrel and capillary. This ΔP_{ent} value can therefore be directly measured from the right bore, which is associated with the calculation of the elongational viscosity (η_E) and elongational strain rate $\dot{\epsilon}$. The second term ΔP_{cap} is associated with the shear deformation and shear viscosity, which can be calculated at the long (left) bore after subtracting ΔP_{ent} . True corrections have been applied to the capillary rheometer data to more accurately describe the non-Newtonian behaviour of the feedstock, namely, the above-mentioned Bagley and Rabinowitsch corrections. Moreover, owing to the high viscosity of the powder-binder feedstock, the assumption of no wall slipping, typical of capillary rheology, is removed. Therefore, the apparent shear rate was corrected as follows:

$$\dot{\gamma} = \dot{\gamma}_a - \dot{\gamma}_0, \quad (9)$$

where $\dot{\gamma}_0$ is an experimental constant determined by the least squares minimisation; this expresses the shear rate reduction owing to a wall slip. The shear viscosity (η_s) is modelled using a power-law equation as a function of the corrected shear strain:

$$\eta_s = K \dot{\gamma}^{n-1}. \quad (10)$$

The right capillary provides a negligible shear resistance, and therefore its pressure reading, the major cause of which is the entrance pressure, can be entirely associated with the elongational viscosity (η_E):

$$\eta_E = \frac{\sigma_E}{\dot{\epsilon}}, \quad (11)$$

where σ_E is the elongational stress at the orifice, and $\dot{\epsilon}$ is the elongational strain rate. The elongational viscosity can also be modelled using a power-law equation as a function of the apparent shear rate:

$$\eta_E = l \dot{\gamma}_a^{y-1}, \quad (12)$$

where l and y are the consistency and sensitivity parameters associated with the elongational viscosity. The elongational strain rate is independent of the capillary length, although the capillary diameter does have an influence. For a given apparent shear rate $\dot{\gamma}_a$, the elongational strain rate can be estimated based on the following:

$$\dot{\epsilon} = \frac{\dot{\gamma}_a}{4}. \quad (13)$$

Under Cogswell's model assumptions, the elongational stress can be calculated as a function of the entrance pressure drop as follows:

$$\sigma_E = \frac{3}{8}(n + 1)\Delta P_{ent}. \quad (14)$$

After substituting the terms η_s , η_E , $\dot{\gamma}$, $\dot{\epsilon}$ and σ_E in Equation (8), the total pressure drop in the left capillary can be finally expressed in the following way:

$$P_{tot} = \Delta P_{cap} + \Delta P_{ent} = \eta_s \dot{\gamma} \frac{4L_l}{D} + \eta_E \dot{\gamma}_a \frac{2}{3(n+1)} = K \dot{\gamma}^n \frac{4L_l}{D} + l \dot{\gamma}_a^y \frac{2}{3(n+1)} \quad (15)$$

3 Materials, equipment, and methods

3.1 Feedstock characterisation

Three different feedstocks were used for this study. A feedstock with a solid loading of stainless steel (SS 316L) powder was prepared by mixing a water-soluble Embemould K83 binder (eMBe, GmbH) and gas-atomised (SS 316L) powder (Sandvik Osprey) in a Brabender-Plasti-Corder mixer. Parenti et al. [29] used the same binder for thermoplastic processing, applying a combination based on polymers with water-soluble components. The binder is specifically devoted to aqueous de-binding for the PIM process. After a DSC analysis, they concluded that it is multi-constituent with three different ingredients and that the highest associated melt temperature is approximately 118 °C. The density of the water-soluble material K83 is 1.05 g/cm³. Mixing of the K83 binder and powder was performed at 145 °C for 30 min to produce a homogeneous feedstock without introducing air bubbles.

This feedstock mixture was further processed through a twin-screw extruder at 145 °C to obtain a highly homogeneous and pelletised feedstock for the subsequent operations. Two commercial (INMATEC, GmbH) ceramic feedstocks, having a solid loading of alumina-based ceramic powder (INMAFEED K1008) and zirconia-based ceramic powder (INMAFEED K1009) were procured. The chemical composition of the stainless steel, alumina, and zirconia powders is shown in Table 1.

In Table 2, the relevant physical and thermal properties of the investigated feedstocks are shown. Physical and thermal properties of the feedstock play an important role in the stability and phase change during extrusion and 3D printing.

All powders used in the present study are fine powders with d_{50} of less than 10 μm , allowing components with a fine microstructure and smooth surface to be produced through the EAM process.

The volumetric powder loading ϕ of the two types of commercial ceramic feedstock were clearly selected by the producer. The powder loading of the steel feedstock with the best value for extrudability was selected according to a previous study [6].

Table 1: Chemical composition (by wt.%) of powders used in the present study

Element	Cr	Ni	Mo	Mn	Si	C	P	S	Fe
SS 316L steel	17.90	11.70	2.30	1.41	0.72	0.02	0.02	0.006	65.7
Compound	Na ₂ O	Fe ₂ O ₃	SiO ₂	Al ₂ O ₃	ZrO ₂	Y ₂ O ₃	MgO	CaO	
Alumina	0.1	0.03	1.8	96	-	-	0.9	1.3	
Zirconia	0.04	0.01%	0.02	0.25	94.5	5.15	-	-	

Table 2: Physical and thermal properties of feedstock used in the present study; d_{50} is the mean diameter of the powder, ϕ is the powder loading (vol%) in the feedstock, and ρ , k , and C_p are the density, thermal conductivity, and heat capacity of the feedstock, respectively.

Feedstock	d_{50} (μm)	ϕ (vol.%)	ρ (kg/m^3)	k (W/m K)	C_p (J/kg K)	α (vol.%)
Al ₂ O ₃ -binder	1.9	60	2,400	0.63	1,528	0.17
ZrO ₂ -binder	0.6	47	2,550	0.43	794	0.21
SS316L-binder	8.8	62	5,320	0.66	1,668	0.07

The thermal conductivity (k) of the feedstock is non-proportional to the solid content (i.e. weight of the powder in the feedstock) because the heat flow is limited by the binder system, with a continuous matrix forming a layer between particles. The thermal conductivity k of each feedstock was calculated using an equation provided by Lobo and Cohen [30]:

$$\frac{1}{k} = \frac{1-\varphi}{k_b} + \frac{\varphi}{k_f}, \quad (16)$$

where φ is the volumetric powder loading, and k_b and k_p are the nominal thermal conductivities of the binder and powder, respectively.

The heat capacity C_p of the feedstock is calculated up to the suggested operational temperature (145 °C for alumina, 175 °C for zirconia, and 130 °C for stainless steel), through an analysis of the DSC curve [31]. The three powders differ considerably in terms of the heat capacity, the estimate of which is also provided in Table 2. The values were measured based on differential scanning calorimetry (DSC) tests, conducted under the ASTM D3418-15 standard, using a differential scanning calorimeter (DSC2010, TA Instruments). The pan was aluminium, and the test was performed in a nitrogen atmosphere, with a gas flow rate of 40 ml/min. The applied heating rate corresponded to 5 °C/min. The DSC curves of the feedstocks are plotted in Fig. 1, which shows a comparison between the curves of the metal and the ceramic feedstock. Both ceramic feedstocks present a peak at the same temperature of 60.8 °C corresponding to the melting point of the industrial binder. However, the stainless steel feedstock presents a single fusion peak at 62.9 °C with a latent heat of fusion of 26.1 J/g. The solidification temperature is observed to be 38.0 °C. The DSC curve also shows indistinct peaks at 64.4 °C, 96.9 °C, 110.5 °C, and 158.3 °C, corresponding to the melting and solidification of different components (PEG, PMMA, surfactants, and additives, respectively) in an Embemould K83 binder.

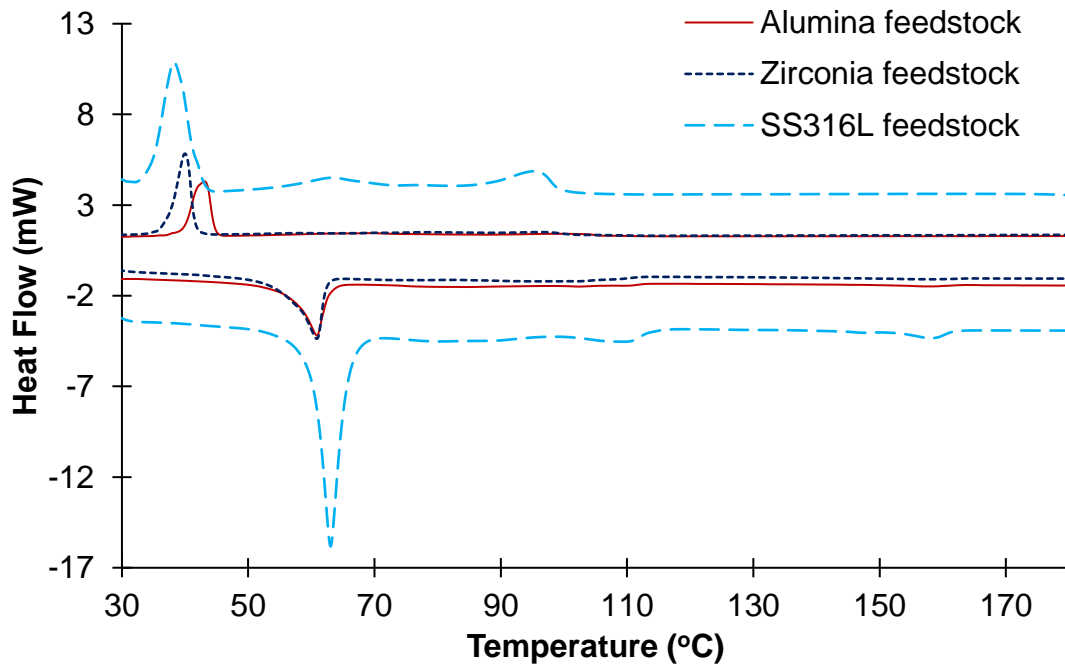


Fig. 1: DSC curves of alumina, zirconia, and stainless steel feedstocks

Once the properties ρ , C_p , and k are known, the diffusivity α can be calculated as a derived variable. Table 2 shows that the thermal diffusivity α of zirconia is the largest (owing to its low heat capacity), followed by alumina, whereas the diffusivity of the steel feedstock is significantly smaller (owing to its higher density).

3.2 Capillary rheometers

The rheological properties of all feedstocks were determined using two different twin-bore capillary rheometers (Fig. 2a), labelled as rheometers A and B (Malvern Panalytical). The selected test temperatures were 145 °C for alumina, 175 °C for zirconia, and 130 °C for stainless steel, over a wide range (50 to 1000 s⁻¹) of shear rates. A sample of each material was positioned in a cylindrical barrel with moving pistons. Defining the piston speed, the material is forced into a long capillary of known diameter D_l and length L_l at the bottom-left of the barrel, and into an extremely short capillary with D_r and L_r on the right. The values of D_r and L_r for both rheometers are given in Fig. 2c and used for the calculations described in Section 4.1 for validation. Pressure transducers are placed immediately above the capillaries; the output of this test is therefore the pressure from each bore. This setup allows the determination of the shear viscosity from the left capillary and the elongational viscosity from the right capillary, according to the model presented above.

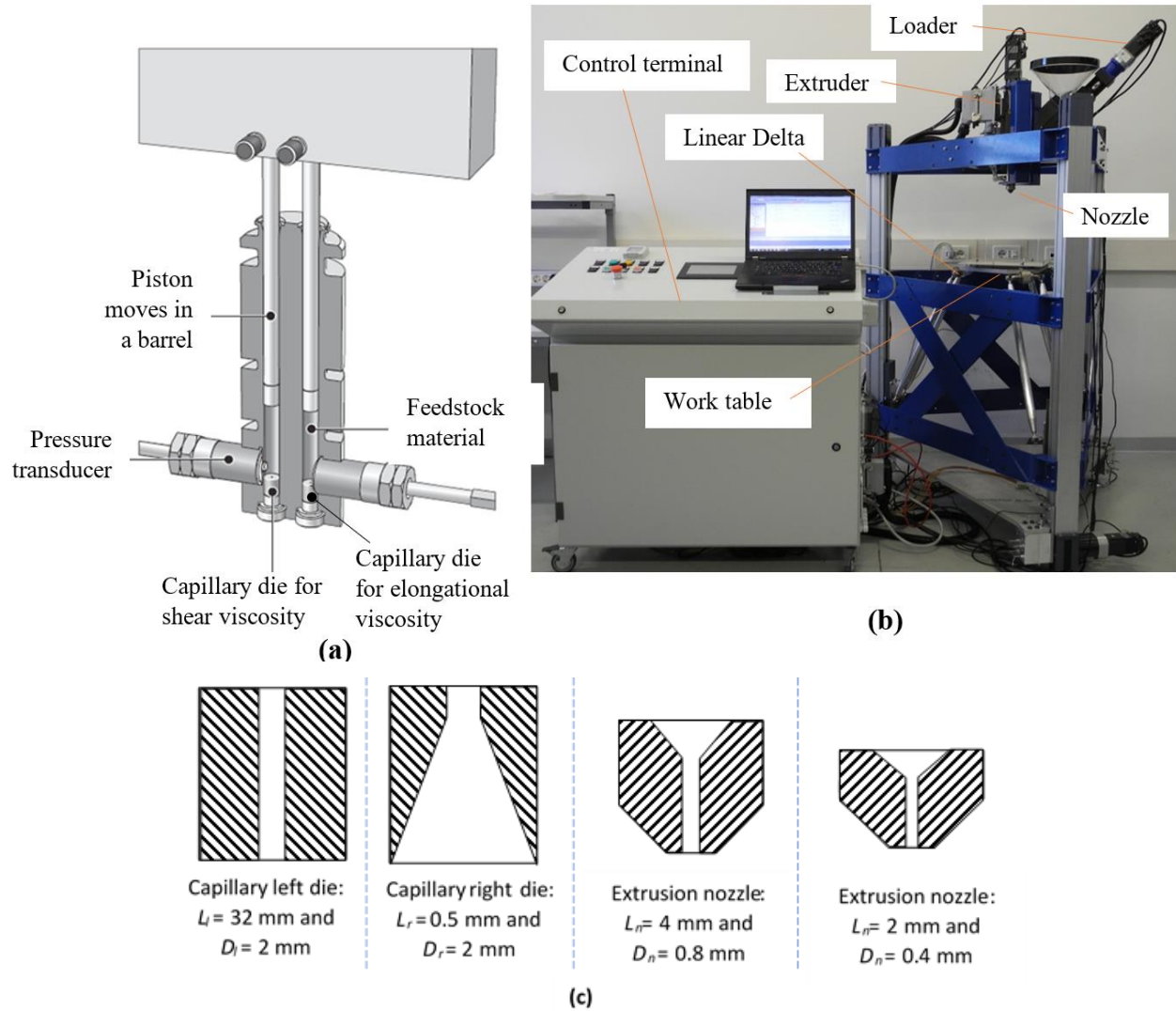


Fig. 2: Main components of (a) capillary rheometer and (b) EFeSTO machine, and (c) schematic of die and nozzles

3.3 Description of specific EFeSTO equipment

The EFeSTO machine, shown in Fig. 2b, has been used both for extrusion and 3D printing tests. The work table is free to move in the X-, Y-, and Z-directions and is governed by a 3-axis parallel kinematics Linear Delta system. The printing head is stationary and composed of a feeder where the pellets of the feedstock are placed, as well as a screw plasticiser and an injector piston. In the extruder system, the feedstock is inserted into the feeder and falls into a first loader chamber, which plasticises the material; it is then injected into a second extruder chamber, where a CNC piston directly pressurises the melt material through the nozzle. For this study, two different nozzles were employed, with a nozzle diameter (D_n) of 0.4 and 0.8 mm, respectively.

Three electric resistors (in the plasticisation chamber, in the extrusion chamber, and at the nozzle) provide heat to the material, and four thermocouples provide a temperature control. Thermal insulation between the high-temperature plasticisation unit and the actuator unit is achieved using a water-cooling circuit. The stroke of the extrusion piston is synchronised with the g-code of the deposition table, and therefore stops during rapid movements of the table, e.g. between consecutive layers of the 3D printed part.

For each experimental run on EFeSTO, the electric current absorbed by the piston drive was recorded and transformed into torque M versus the time signal. Data from the extruder motor was collected using Melsoft MR Configurator software. The data were stored in a local memory support, and owing to the length of the operations, a continuous pressure reading was considered infeasible. Therefore, data were collected during intervals of 50 s each at different times throughout the tests. The sampling frequency was 20 Hz. During the extrusion and 3D printing tests, the torque measurements were conducted more frequently at the beginning and end of the tests, with 2 min between consecutive readings. In the central part of each test, the torque was measured with a longer time between readings: 10 min for extrusion and 5 min for 3D printing. The torque M versus time signals were then converted into pressure P_{tot} signals.

Among the individual samples of the pressure readings, the average total pressure P_{tot} was calculated along with the standard deviation SD_P and coefficient of variation $COV_P = P_{tot}/SD_P$. As an example, in Fig. 3, P_{tot} is plotted versus time during a sequence of extrusion and printing tests. The typical long-run trend of the pressure signal undergoes an initial increase in pressure, stabilisation, and a marginal increase at the end of the piston stroke. This is coherent with the flow of pseudoplastic fluids: The initial increase corresponds to an activation of the flow, and stabilisation occurs because of the steady state extrusion regime. The pressure increase at the end of the stroke likely occurs because the piston attempts to extrude the material, which forms a dead zone at the corners of the extrusion chamber.

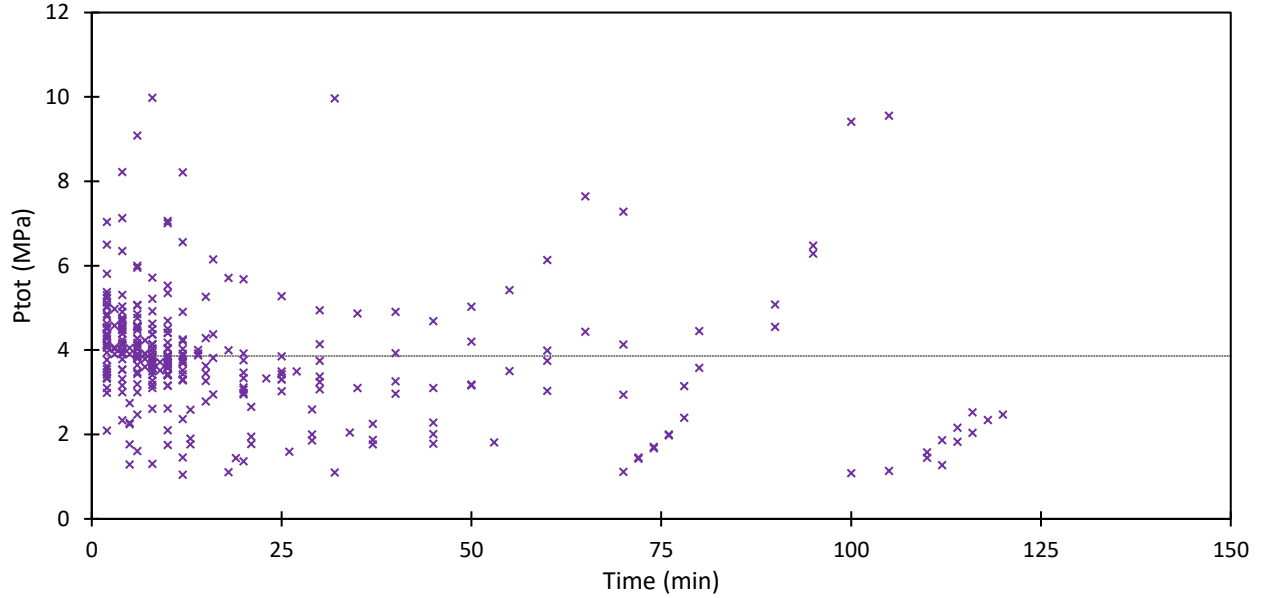


Fig. 3: Sequence of pressure readings for extrusion pressure (P_{tot}) of stainless-steel feedstock: average measured pressure $P_{tot} = 3.86$ MPa with coefficient of variation $COV_P = 8.1\%$

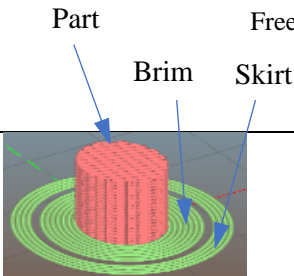
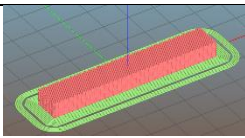
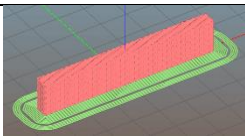
3.4 Experimental plan implemented using EFeSTO

Two main types of tests were conducted: free continuous extrusion tests and 3D printing tests. During each test, as described before, the average extrusion pressure at piston P_{tot} , as well as its standard deviation SD_P and coefficient of variation COV_P , were recorded at regular intervals. Whereas during continuous extrusion the extrusion piston moves at a constant speed, during real 3D printing it experiences multiple starts and stops, which might influence the measured values of SD_P . For each feedstock, three different shapes were 3D printed (shown in Table 3): cylinders with a base diameter of 10 mm and a height of 10 mm, and bars with a rectangular cross section with a 6 mm height, 60 mm length, and 10 mm width. The rectangular bars were printed in both a horizontal and vertical configuration, placed on a face with dimensions of 60 mm \times 10 mm.

The parameter settings used for extrusion and 3D printing tests, and designed to produce different apparent shear rates, are given in Table 3, namely two nozzle diameters D_n , three extrusion velocities V_e , three materials, and four types of test. The layer height h does not have an influence on the pressure readings, and therefore is not listed in Table 3; however, it was varied around a centre value of half the nozzle diameter. A full factorial experimental plan would have required 72 different experimental conditions, plus replicates. Table 3 lists only 31 out of 72 possible experimental conditions, which were used to keep the experimental cost within a reasonable limit. The 31 tested conditions were replicated a minimum of 2 and

a maximum of 5 times, for a total of 184 different tests. Multiple pressure readings were recorded during each test, resulting in the availability of a very large dataset.

Table 3: Experimental plan for extrusion and 3D printing tests

Shape/Test	Material	Extrusion velocity V_e (mm/s)		
		7.5	12.5	17.5
		D_n (mm)	D_n (mm)	D_n (mm)
 Free Extrusion Cylinder	Al_2O_3	0.4	0.4	0.4
	SS 316L	0.4–0.8	0.4–0.8	
	ZrO_2			
 Rectangular horizontal bar	Al_2O_3	0.4	0.4	0.4
	SS 316L	0.4–0.8	0.8	0.8
	ZrO_2	0.8	0.8	0.8
 Rectangular vertical bar	Al_2O_3	0.4	0.4	0.4
	SS 316L	0.4		
	ZrO_2	0.8	0.8	0.8

4 Results and discussion of rheological data

The rheological models given in Equations (9), (10), and (12) were applied to the capillary rheometer data (through linear regression). The corresponding material parameters ($\dot{\gamma}_0$, K , n , l , and y) are provided in Table 4.

Table 4: Power-law parameters and correction shear rate for the three feedstocks

Feedstock	K (Pa.s)	n	l (kPa.s)	y	$\dot{\gamma}_0$ [s^{-1}]
SS316L	1,187	0.678	1,530	0.133	16
Alumina	5,219	0.279	1,086	0.210	1
Zirconia	3,622	0.592	6,568	0.050	7

The values of consistency l of the elongational viscosity are three orders of magnitude higher than the shear viscosity consistency K at a comparable strain rate. This means that the ratio of the elongational viscosity function to the shear viscosity function is high, corresponding to a Trouton ratio of η_E/η_s . This Trouton ratio is approximately 100 in the case of 316L feedstock and 200 s^{-1} .

The consistency K of the SS316L steel feedstock is significantly smaller than that of the other two materials at lower than 1,200 Pa.s. Indeed, to verify the flow stability, samples of the extruded SS316L feedstock were collected at a shear rate of approximately 600 s^{-1} . The surfaces of the rods are shown in Fig. 4 (a) and (b). For the left (longer) capillary, the quality observed at the outer surface of the rod is smooth, whereas the capillary extruded from the right (shorter) shows a sharkskin defect. This type of instability can be observed in a polymer extrusion when the capillary/nozzle length is extremely small ($L \approx 0$) and is connected with a rapid detachment of the melt flow at the exit of the capillary [32]. This sharkskin problem has previously been observed for EAM processes [33].

The rheological models can be applied to the conditions of the planned extrusion and 3D printing tests (given in Table 3), and the corresponding expected feedstock viscosities at the nozzle can be estimated. A comparison of the shear and extensional viscosity characteristics of the three high-loaded polymers corresponding to the extrusion and 3D printing test settings was conducted. In Fig. 5, a comparison between the shear and elongational viscosity is shown for all studied combinations. In the nozzle with $D_n = 0.8$ mm a lower shear rate is clearly calculated. The shear rate tested with the alumina is larger owing to its lower n -value, which determines a stronger Rabinowitsch correction.

The elongational viscosity of the zirconia feedstock is significantly larger than that of the other two materials as compared to the shear viscosity, which is due to the larger elongational consistency l for zirconia of greater than 6500 kPa.s.

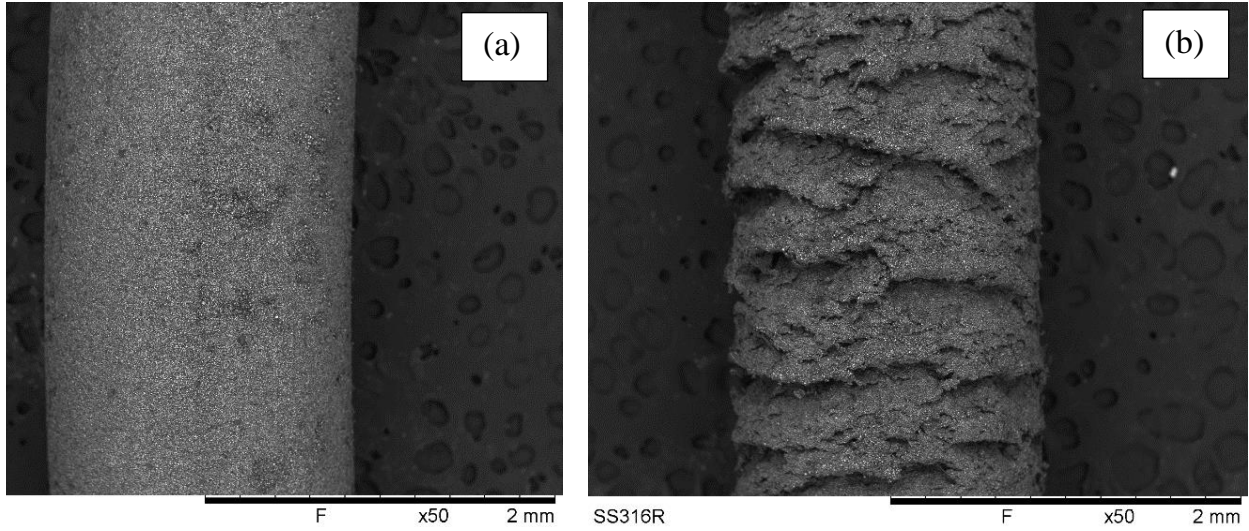


Fig. 4: Extruded roads of SS316L feedstock from (a) left and (b) right capillaries at shear rate of 600 s^{-1}

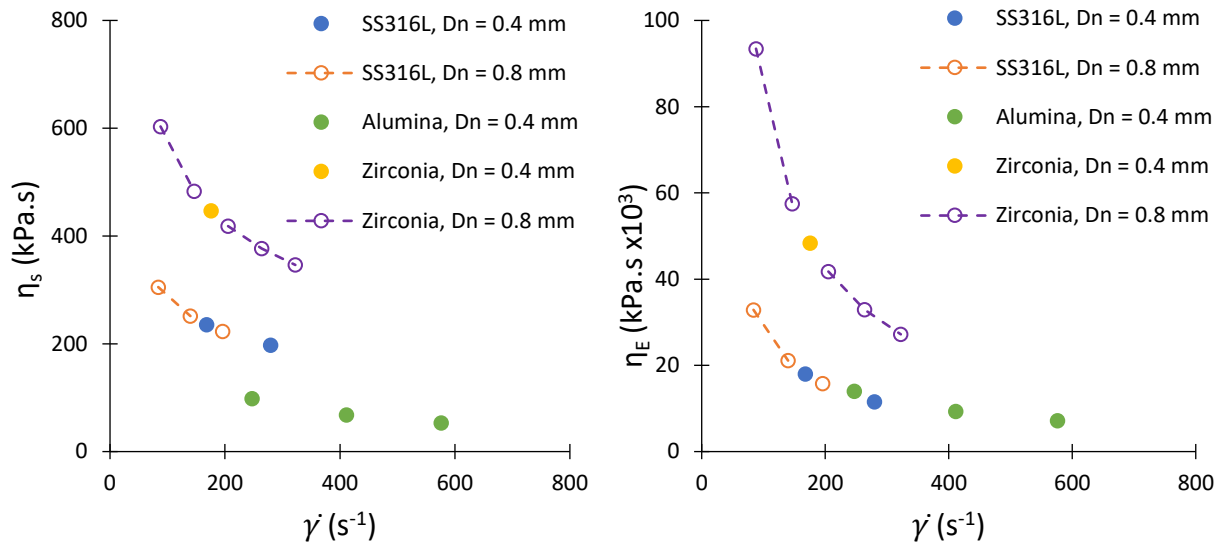


Fig. 5: Shear and elongational viscosity of three feedstocks versus shear rate corresponding to extrusion and 3D printing test settings

4.1 Validation of pressure drop model

The pressure drop model presented in Equation (15) can be applied inversely, and if the viscosity values are known, the total pressure drops can be calculated. The rheological parameters given in Table 4 for the stainless steel feedstock were obtained from a Rosand capillary rheometer (rheometer A, $L_l = 17 \text{ mm}$, $L_r \approx$

0 and $D_l = D_r = 1$ mm), and were used to predict the total pressure P_{tot} required when using another rheometer with a different capillary configuration (rheometer B, $L_l = 32$ mm and $D_l = D_r = 2$ mm). In Fig. 6 the predicted pressure is compared to the test with equipment B, showing a good agreement. Rheometer B has a double length in the left capillary, but with nearly the same L_l/D_l ratio, and hence the pressure requirement owing to the shear viscosity is similar. By contrast, the right bore of rheometer B has a double diameter and requires a significantly lower pressure ΔP_{right} owing to the elongational viscosity. In conclusion, the total pressure required by rheometer B is up to 40% smaller, primarily because of the elongational viscosity. This is an important confirmation of the important role of the elongational viscosity in the extrusion of powder-binder feedstocks.

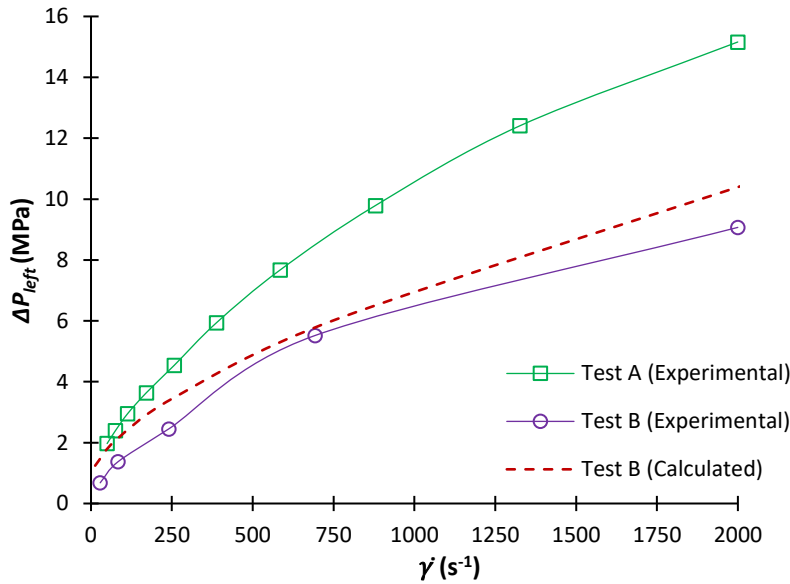


Fig. 6: Experimental and calculated $P_{tot} = \Delta P_{left}$ for different capillary configurations and strain rates

5 Results of extrusion and 3D printing tests

The methodology used for predicting $P_{tot} = \Delta P_{left}$ with Equation (15) at the left-side capillary rheometer can also be adapted to predict the total extrusion pressure during extrusion and 3D printing tests on an EFeSTO machine. The extrusion unit is geometrically complex, and can be reconducted into a series of cylindrical capillaries, the pressure drops of which can be estimated using Equation (15).

Fig. 7 shows a cross section of the flow channels of the extruder, with the respective pressure drop in the channels during the feedstock flows shown on the right side. From the main extruder chamber (A), the material flow is divided into two identical sections (B), which are further split into two long tubes (C) from each section. The material flow from these four channels flows into the nozzle region (D).

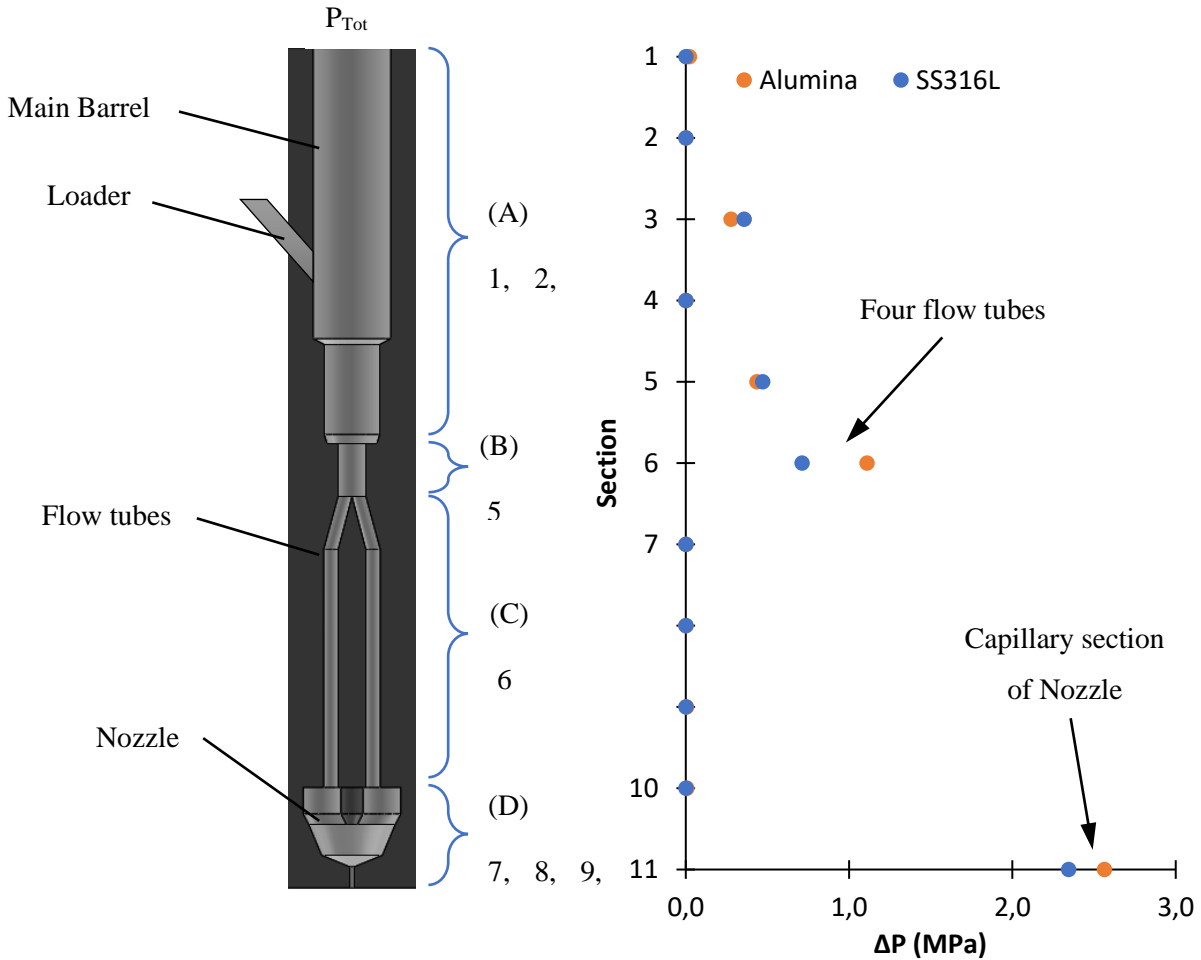


Fig. 7: Simplified cross-sectional view of extrusion system and flow channels used for feedstock

The cross-sectional area of the flow channels also accounts for the determination of the pressure drop through the extrusion unit, and is subdivided into 11 zones with simple geometries. The elongational fraction of Equation (15), ΔP_{ent} , has been computed only for the entrance of sections 3, 5, 6, and 11 because these sections represent a restriction of the flow. In the shear fraction of Equation (15), ΔP_{cap} has been measured at all sections after section 2, but is significant only at sections 6 and 11 because of the extremely high aspect ratio L/D_n . The right side of Fig. 7 shows a representative plot of the pressure drop across the 11 sections measured at $V_e = 12.5$ mm/s and $D_n = 0.4$ mm for the alumina and steel feedstocks.

The total pressure drops under all experimental conditions were measured and compared to the experimental values. This comparison is summarised in Fig. 8, which shows that the measured pressure (P_{tot}) and the calculated pressure components ΔP_{cap} and ΔP_{ent} increase linearly with an extrusion at velocity V_e because of the larger flow rate.

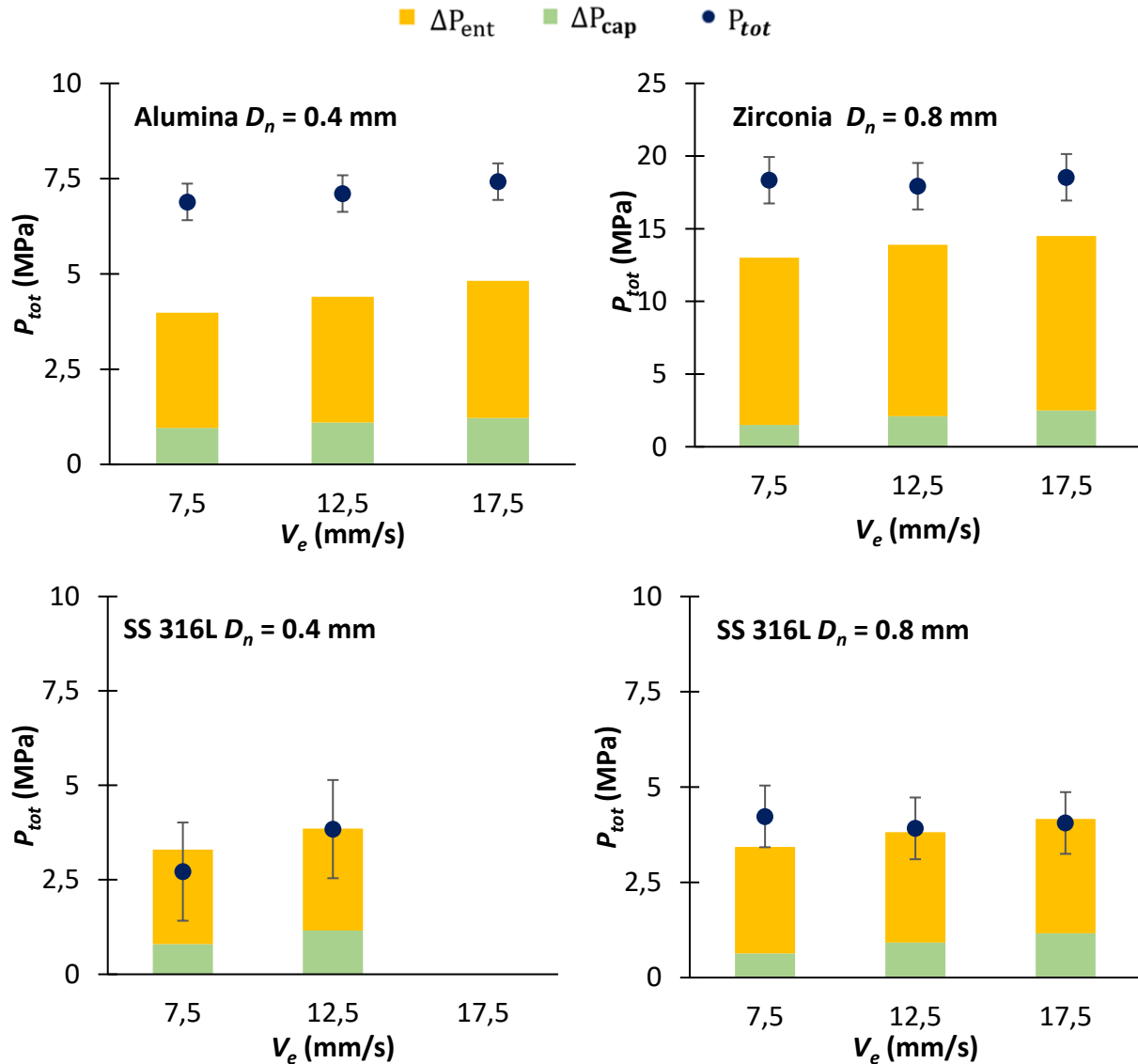


Fig. 8: Experimental and calculated extrusion pressures for different feedstocks and extrusion velocities; error bars are plotted equal to the pooled standard deviation of the V_e values of each graph

Zirconia requires more than double the pressure required by the alumina and SS316L. The alumina feedstock P_{tot} requires between 6 and 8 MPa of pressure, whereas the SS316L feedstock requires P_{tot} at below 6 MPa. The predicted pressures properly capture the actual measure pressured for stainless steel, whereas they underestimate the actual pressure requirements of the two ceramic materials. This

underestimation is probably connected with the different thermal value of the ceramic feedstock (having a larger thermal diffusivity, as shown in Table 2), and they likely cool faster than the steel as soon as they approach the exit of the nozzle, with a viscosity increase that cannot be captured by the model inside the extrusion unit. Although the model underestimates P_{tot} for the ceramic feedstocks, it clearly gives an indication of the relative importance of the shear ΔP_{cap} and elongational ΔP_{ent} components of the pressure. Here, ΔP_{cap} is significantly larger for all cases, as further proof of the dramatic importance of the elongational deformation, rather than the shear deformation, during the EAM processes of highly viscous feedstocks.

5.1 Quality and stability of the extrusion and 3D printing process

A complete representation of the mechanical and geometrical sintered properties of the 3D printed ceramic materials is not the main focus of the present paper, which is aimed at the consequences of the rheology of viscous melts on the pressure values. Previous results of the sintering properties regarding this aspect are available in [34] and [35]. In the section, the correlation between the variability of the pressure signal and the variability of sintered quality is investigated.

As shown in Table 3, several samples of different shapes have been 3D printed in their green state, i.e. when the powder is mixed into the thermoplastic polymeric binder. The pressure signals during each test were recorded, along with their coefficients of variation COV_P (the ratio between the standard deviation of each pressure sample and the mean sampled pressure). The results were statistically analysed and clearly show that COV_P depends on the feedstock material, with stainless steel being significantly less stable than zirconia and alumina. By contrast, the error COV_P in the pressure signal measured using the four different types of printing (free extrusion, cylinder, horizontal prismatic bar, and vertical prismatic bar) did not show any clear differences, with a random ranking among the different shapes. This is effectively shown through Fig. 9. The reason for the lower stability of the steel is probably connected to its lower consistency K , as a confirmation of previous findings [6]. Interestingly, there seems to be no correlation between the shear rate and the stability COV_P of the pressure signal.

After 3D printing, some of the samples underwent de-binding and were sintered to better understand the variations in their surface quality characteristics. Because this study is focused on the extrusion pressure, the parts were printed without outer contour roads to enhance the variations owing to the start and stops and directional changes. All samples therefore show an extremely rough surface finish in a green state, which mildly improves after sintering. Representative 3D printed parts in their green and sintered states are shown in Fig. 10, and their sintered properties are reported in Table 5.

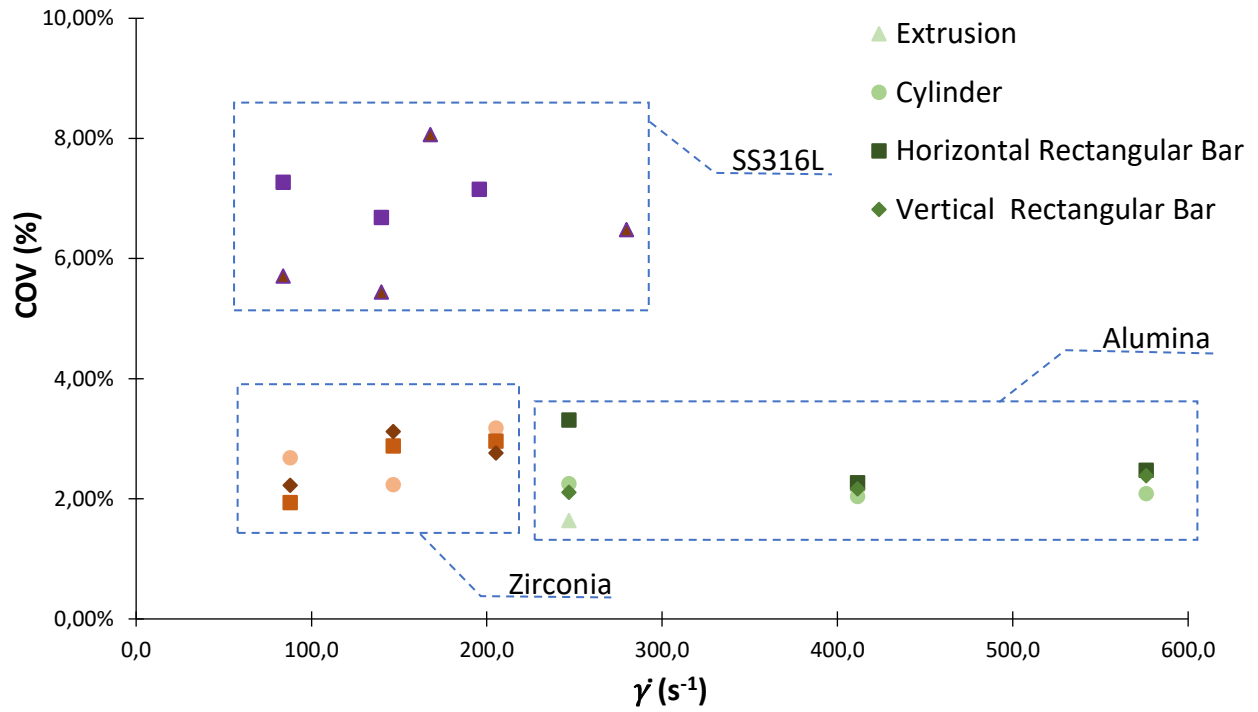


Fig. 9: Coefficient of variation COV_p of the pressure signal for the different types of tests and materials.

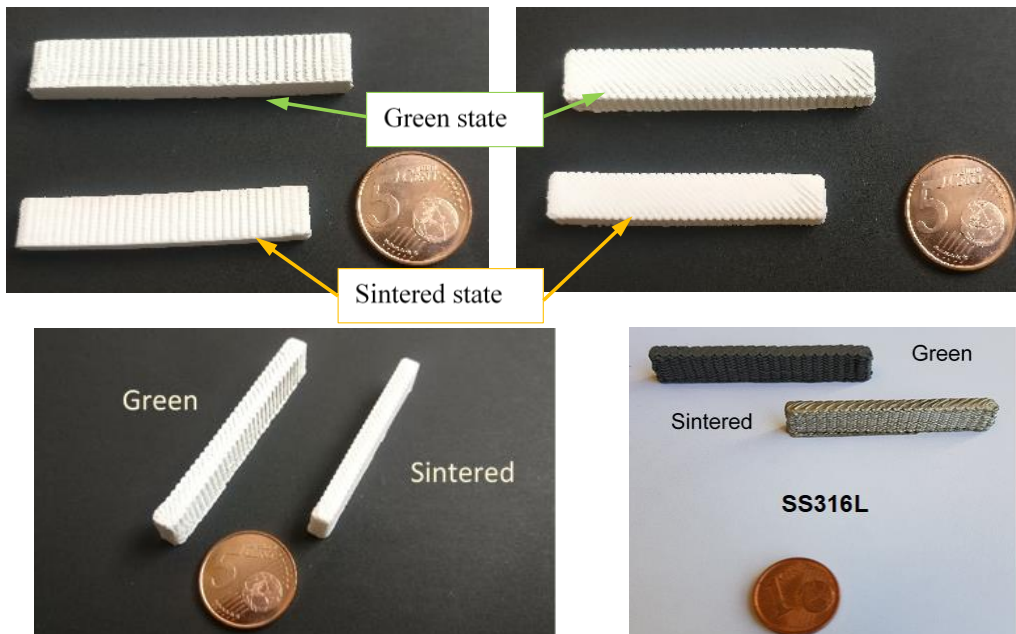
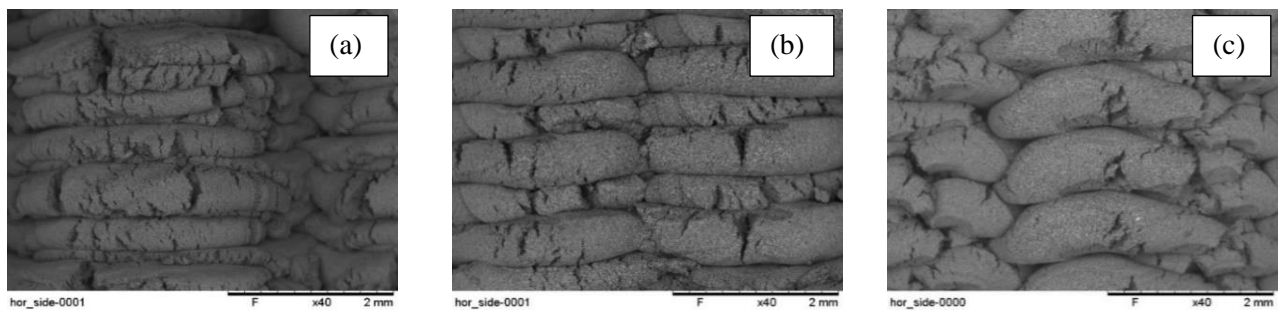


Fig. 10: Green and sintered alumina in rectangular bar-shaped parts printed in a vertical (top-left) and horizontal (top-right) configuration, and green and sintered steel (bottom-right) and zirconia (bottom left) parts

Table 5: Sintered properties of alumina, zirconia, and S316L at extrusion speed of 12.5 mm/s

Material	Alumina	Zirconia	SS316L
Density (g/cm ³)	3.60	5.65	7.11
Elastic Modulus (GPa)	81.5	27.33	77.26

Owing to the sintering, shrinkage reduces the waviness on the surface, although the structure of the surface texture remains unchanged. To further recognise the role of the printing parameters on the surface quality, surface characteristics of 3D printed components are also analysed using SEM. The observations indicate that the surface quality of the components is not correlated with COV_p and depends only on the material to be printed and on the infill and layering parameters, as is well-known for all EAM processes. As an example, Fig. 11 (a–c) compares the surface characteristics of green SS316L samples printed with different layer heights h . Because the surface quality of the parts is not influenced by the variations in pressure, a quantitative report of the surface quality data is omitted herein for brevity. Zhou et al. developed some numerical optimisation approaches to increase the tensile strength and control the volumetric shrinkage values through different cost functions dedicated to the polymer FFD process, and optimised the processing parameters [36]. This promising method will be adapted in the future. An estimation of the shrinkage is a real challenge in additive manufacturing, and Fotovvati et al. proposed an analytical expression to quantify the size dependency of the dimensional percentage errors with a polynomial function in the DMLS manufactured features [37]. This methodology will be adjusted during the FFD process in the future.

**Fig. 11:** SEM images for side walls of SS316L samples, printed with a 0.8 mm nozzle and different printed layer heights h of (a) 0.3, (b) 0.4, and (c) 0.5 mm

6 Conclusions

This work is focused on the measurement and prediction of the instantaneous pressure occurring during the extrusion and EAM operations of highly viscous powder–binder feedstocks. A pressure prediction model was developed when considering both the shear and elongational viscosity contributions. The material parameters were calculated from capillary rheometry data, which were also used to validate the model by verifying its agreement with the experimental viscosity measurements.

An extensive extrusion plan and 3D printing tests were applied to three different materials (steel, alumina, and zirconia) over a range of different nozzle diameters, extrusion velocities, and 3D printed shapes. The results indicate that the pressure requirements owing to the elongational viscosity are dominant with respect to the contributions of the shear viscosity.

The results also indicate that, among the investigated parameters, the stability of the pressure signals depend on the material feedstock and not on the shear rate or shape of the 3D printed parts.

7 References

- [1] Royer A, Barrière T, Gelin JC. Development and characterization of a metal injection molding bio sourced inconel 718 feedstock based on polyhydroxyalkanoates. *Metals (Basel)* 2016;6. <https://doi.org/10.3390/met6040089>.
- [2] Rane K, Strano M. A comprehensive review of extrusion-based additive manufacturing processes for rapid production of metallic and ceramic parts. *Adv Manuf* 2019;7:155–73. <https://doi.org/10.1007/s40436-019-00253-6>.
- [3] Chen Z, Li Z, Li J, Liu C, Lao C, Fu Y, et al. 3D printing of ceramics: A review. *J Eur Ceram Soc* 2019;39:661–87. <https://doi.org/10.1016/j.jeurceramsoc.2018.11.013>.
- [4] Nadernezhad A., Unal S., Khani N. KB. Material extrusion-based additive manufacturing of structurally controlled poly(lactic acid)/carbon nanotube nanocomposites. *Int J Adv Manuf Technol* 2019;102:2119–2132.
- [5] Annoni M, Giberti H, Strano M. Feasibility Study of an Extrusion-based Direct Metal Additive Manufacturing Technique. *Procedia Manuf* 2016;5:916–27. <https://doi.org/10.1016/j.promfg.2016.08.079>.
- [6] Strano M, Rane K, Briatico Vangosa F, Di Landro L. Extrusion of metal powder-polymer mixtures: Melt rheology and process stability. *J Mater Process Technol* 2019;273:116250. <https://doi.org/10.1016/j.jmatprotec.2019.116250>.
- [7] J.Hidalgo, A.Jiménez-Morales, T.Barriere, J.C.Gelin, J.M.Torralba. Capillary rheology studies of INVAR 36 feedstocks for powder injection moulding. *Powder Technol* 2015;273:1–7. <https://doi.org/10.1016/j.powtec.2014.12.027>.
- [8] Dimitri C, Mohamed S, Thierry B, Jean-Claude G. Influence of particle-size distribution and temperature on the rheological properties of highly concentrated Inconel feedstock alloy 718. *Powder Technol* 2017;322:273–89. <https://doi.org/10.1016/j.powtec.2017.08.049>.

- [9] Rane K, Di Landro L, Strano M. Processability of SS316L powder - binder mixtures for vertical extrusion and deposition on table tests. *Powder Technol* 2019;345:553–62. <https://doi.org/10.1016/j.powtec.2019.01.010>.
- [10] N. Turner B, Strong R, A. Gold S. A review of melt extrusion additive manufacturing processes: I. Process design and modeling. *Rapid Prototyp J* 2014;20:192–204. <https://doi.org/10.1108/RPJ-01-2013-0012>.
- [11] Mackay ME. The importance of rheological behavior in the additive manufacturing technique material extrusion. *J Rheol (N Y N Y)* 2018;62:1549–61. <https://doi.org/10.1122/1.5037687>.
- [12] Singh P, Shaikh Q, Balla VK, Atre S V, Kate KH. Estimating Powder-Polymer Material Properties Used in Design for Metal Fused Filament Fabrication (DfMF 3). *JOM* 2019. <https://doi.org/10.1007/s11837-019-03920-y>.
- [13] Faes M, Vleugels J, Vogeler F, Ferraris E. Extrusion-based additive manufacturing of ZrO₂ using photoinitiated polymerization. *CIRP J Manuf Sci Technol* 2016;14:28–34. <https://doi.org/10.1016/j.cirpj.2016.05.002>.
- [14] Kukla C, Gonzalez-Gutierrez J, Duretek I, Schuschnigg S, Holzer C. Effect of particle size on the properties of highly-filled polymers for fused filament fabrication. *AIP Conf Proc* 2017;1914. <https://doi.org/10.1063/1.5016795>.
- [15] Khaliq MH, Gomes R, Fernandes C, Nóbrega J, Carneiro OS, Ferrás LL. On the use of high viscosity polymers in the fused filament fabrication process. *Rapid Prototyp J* 2017;23:727–35. <https://doi.org/10.1108/RPJ-02-2016-0027>.
- [16] Coogan TJ, Kazmer DO. In-line rheological monitoring of fused deposition modeling. *J Rheol (N Y N Y)* 2019;63:141–55. <https://doi.org/10.1122/1.5054648>.
- [17] Thavanayagam G, Pickering KL, Swan JE, Cao P. Analysis of rheological behaviour of titanium feedstocks formulated with a water-soluble binder system for powder injection moulding. *Powder Technol* 2015;269:227–32. <https://doi.org/10.1016/j.powtec.2014.09.020>.
- [18] Khakbiz M, Simchi A, Bagheri R. Analysis of the rheological behavior and stability of 316L stainless steel–TiC powder injection molding feedstock. *Mater Sci Eng A* 2005;407:105–13. <https://doi.org/10.1016/j.msea.2005.06.057>.
- [19] Park SJ, Kim D, Lin D, Park SJ, Ahn S. Rheological characterization of powder mixture including a space holder and its application to metal injection molding. *Metals (Basel)* 2017;7. <https://doi.org/10.3390/met7040120>.
- [20] Huang B, Liang S, Qu X. The rheology of metal injection molding. *J Mater Process Technol* 2003;137:132–7. [https://doi.org/10.1016/S0924-0136\(02\)01100-7](https://doi.org/10.1016/S0924-0136(02)01100-7).
- [21] Samanta SK, Chattopadhyay H, Godkhindi MM. Thermo-physical characterization of binder and feedstock for single and multiphase flow of PIM 316L feedstock. *J Mater Process Technol* 2011;211:2114–22. <https://doi.org/10.1016/j.jmatprotec.2011.07.008>.
- [22] Huang JC, Leong KS. Shear viscosity, extensional viscosity, and die swell of polypropylene in capillary flow with pressure dependency. *J Appl Polym Sci* 2002;84:1269–76. <https://doi.org/10.1002/app.10466>.
- [23] Aho J, Syrjälä S. Shear viscosity measurements of polymer melts using injection molding machine with adjustable slit die. *Polym Test* 2011;30:595–601. <https://doi.org/10.1016/j.polymertesting.2011.04.014>.
- [24] Ohtani H, Ellwood K, Pereira G, Chinen T, Selvasekar S. Extensional Rheology: New Dimension of Characterizing Automotive Fluids. *SAE Tech Pap* 2017;2017-March.

<https://doi.org/10.4271/2017-01-0364>.

- [25] Cogswell FN. Measuring the Extensional Rheology of Polymer Melts. *Trans Soc Rheol* 1972;16:383–403. <https://doi.org/10.1122/1.549257>.
- [26] Zatloukal M, Musil J. Analysis of entrance pressure drop techniques for extensional viscosity determination. *Polym Test* 2009;28:843–53. <https://doi.org/10.1016/j.polymertesting.2009.07.007>.
- [27] Hong SY, Broomer M. Economical and ecological cryogenic machining of AISI 304 austenitic stainless steel. *Clean Prod Process* 2000;2:0157–66. <https://doi.org/10.1007/s100980000073>.
- [28] Arabo EYM. Shear and extensional viscosities of hard wheat flour dough using a capillary rheometer. *J Food Eng* 2011;103:294–8. <https://doi.org/10.1016/j.jfoodeng.2010.10.027>.
- [29] Parenti P, Cataldo S, Grigis A, Covelli M, Annoni M. Implementation of hybrid additive manufacturing based on extrusion of feedstock and milling. *Procedia Manuf* 2019;34:738–46. <https://doi.org/10.1016/j.promfg.2019.06.230>.
- [30] Heaney DF. *Handbook of Metal Injection Molding*. 1st ed. Woodhead Publishing; 2012.
- [31] Liu ZY, Loh NH, Tor SB, Khor KA. Characterization of powder injection molding feedstock. *Mater Charact* 2003;49:313–20. [https://doi.org/10.1016/S1044-5803\(02\)00282-6](https://doi.org/10.1016/S1044-5803(02)00282-6).
- [32] Vergnes B. Extrusion Defects and Flow Instabilities of Molten Polymers. *Int Polym Process* 2015;30:3–28. <https://doi.org/10.3139/217.3011>.
- [33] Kishore V, Ajinjeru C, Liu P, Lindahl J, Hassen A, Kunc V, et al. Predicting Sharkskin Instability in Extrusion Additive Manufacturing of Reinforced Thermoplastics. *Solid Free Fabr Symp* 2017:1696–704.
- [34] Rane K, Petró S, Strano M. Evolution of porosity and geometrical quality through the ceramic extrusion additive manufacturing process stages. *Addit Manuf* 2020;32:101038. <https://doi.org/10.1016/j.addma.2020.101038>.
- [35] Strano M, Rane K, Herve G, Tosi A. Determination of process induced dimensional variations of ceramic parts, 3d printed by extrusion of a powder-binder feedstock. *Procedia Manuf* 2019;34:560–5. <https://doi.org/10.1016/j.promfg.2019.06.220>.
- [36] Zhou X, Hsieh S.J WJC. Accelerating extrusion-based additive manufacturing optimization processes with surrogate-based multi-fidelity models. *Int J Adv Manuf Technol* 2019;103:4071–4083.
- [37] Fotovvati B AE. Size effects on geometrical accuracy for additive manufacturing of Ti-6Al-4V ELI parts. *Int J Adv Manuf Technol* 2019;104:2951–2959.